PCCP

PAPER

View Article Online
View Journal | View Issue

Cite this: *Phys. Chem. Chem. Phys.*, 2025, **27**, 22039

Highly anisotropic electronic properties of the $GdBa_2Ca_2Fe_5O_{13}$ oxide: a DFT+*U* study of a potential air electrode for solid oxide fuel cells

Boris Politov, *[a] Igor Shein[b] and Susana Garcia-Martin *[a]

Received 13th May 2025,
Accepted 22nd September 2025

DOI: 10.1039/d5cp01780g

rsc.li/pccp

Profound knowledge of the electronic structure of functional solids is essential to understand and optimize their properties. The current advances in electronic structure theory, together with the improvements in computing power, allow realization of affordable calculations of the electronic structure of complex solids with the aim of explaining or predicting properties of singular materials. This work presents a density functional theory study of the $GdBa_2Ca_2Fe_5O_{13}$ oxide, a potential air electrode for solid oxide fuel cells with a layered-perovskite-related structure, which presents ordering of three different coordination-polyhedra around the Fe^{3+} ion (FeO_6 octahedra, FeO_5 squared pyramids and FeO_4 tetrahedra). The existence of these three different Fe^{3+}-environments significantly impacts the electronic properties of this oxide leading to a narrow band gap. The band structure calculations of $GdBa_2Ca_2Fe_5O_{13}$ concludes that the FeO_5 layers create the CB (conduction band), the FeO_6-layers form the VB (valence band) and the FeO_4 layers create insulating channels, leading to anisotropic electrical properties that coincide with the experimentally observed 2D magnetic, electrical, and structural characteristics of $GdBa_2Ca_2Fe_5O_{13}$.

1. Introduction

Research on materials oriented towards technological applications is one of the most valuable areas in solid state chemistry and materials science. In this context, metal oxides with perovskite-type crystal structures (ABO_3 stoichiometry) constitute prominent archetypes of functional materials, since they display an extraordinary wide range of electronic properties.[1] The cubic perovskite structure can be described as a corner-linked BO_6-octahedra network with the A-atoms located in 12-coordinated sites formed by four linked octahedra. Transition metal atoms are located at the B-sites while the A-sites are commonly occupied by alkaline-earth metals or lanthanides. The electronic properties of the perovskites are tuned by partial or total substitution of ions into the A and B-sites, sometimes combined with creation of defects such as cation or anion-vacancies. As a consequence, metals, insulators and materials with metal–insulator transitions, also presenting noticeable magnetic properties, are found among different perovskite-related families.[2–5] Perovskite-related oxides have gained a great deal of attention in the field of so-called energy-applications.[6–8] In this regard, numerous perovskites have been studied as electrodes for solid oxide cells, both for fuel cells and electrolyzers (SOFCs and SOECs).[9–14] Particularly interesting are the mixed-conducting non-stoichiometric layered-perovskites, as for instance those of the system $LnBaCo_2O_{6-\delta}$ (Ln = lanthanide metal), with ordering of Ln and Ba in alternated layers along the [001] direction of the structure.[14–19] Layered-type ordering of Ln and Ba in the crystal structure seems to be crucial to the location of the anion vacancies within the $LnO_{1-\delta}$ planes, creating a higher ionic conductivity than in perovskites with the anion vacancies placed at random in the structure.[20,21] The high demand of Co-materials for energy applications and the low thermal stability of the $LnBaCo_2O_{6-\delta}$ systems associated with their rapid oxygen release/up-taking makes it essential to develop new Co-free perovskites. Substitution of Co by other transition metals in the abovementioned layered-perovskites improves thermal stability, although in general decreases the electronic conductivity, while the ordering in both cationic and anionic sublattices can be modified.[22–24] The ordering of the A-site cations is not only assisted by differences between their ionic radii and oxidation states but also depends on the type and oxidation state of the B-site cations, which highly affect the oxygen content of the compound. Thus, layered-ordering of Gd and Ba in $GdBaMnFeO_{6-\delta}$ is only achieved by using a reducing atmosphere in the first step of the synthesis;[25,26] in a similar way, Pr/Ba ordering in $PrBaFe_2O_{6-\delta}$ requires synthesis under reducing conditions.[27]

[a] *Universidad Complutense de Madrid, Madrid, 28040, Spain.*
E-mail: bpolitov@ucm.es, sgmartin@quim.ucm.es
[b] *Institute of Electrophysics of the UB RAS, Yekaterinburg, 620016, Russia*

Coupling of cation and anion-vacancy orderings to form perovskite-based superstructures is clearly perceived in some complex Fe^{3+}-perovskites, where the Fe^{3+} cations can adopt different oxygen coordination.[28,29] Thought provoking is the modulation of the nuclear and magnetic structures in the $Ln_{0.8-x}Ba_{0.8}Ca_{0.4+x}Fe_2O_{6-\delta}$ systems (Ln = Gd, Tb).[30,31] Three single-phase oxides have been isolated in the system, which are better formulated as $Ln_{1.2}Ba_{1.2}Ca_{0.6}Fe_3O_8$, $Ln_{2.2}Ba_{3.2}Ca_{2.5}Fe_8O_{21}$ and $LnBa_2Ca_2Fe_5O_{13}$ (corresponding to x = 0.00, 0.25 and 0.40 respectively) in agreement with their oxygen content; the compounds constitute the $A_{3m+5n}Fe_{3m+5n}O_{8m+13n}$ homologous series with m and n values 1, 0; 1, 1; and 0, 1, respectively. These three complex perovskite-related oxides present different layered-ordering of the A-site cations in combination with different oxygen-coordination environments around the Fe^{3+} atoms (octahedra, tetrahedra and squared pyramids) along the stacking c-axis. In the system, substitution of Ln^{3+} by Ca^{2+} decreases the oxygen content, which is accommodated by formation of FeO_5-squared pyramid layers intercalated with one A-layer containing mainly Ln^{3+} cations. Like in layered Co-perovskites,[20,21] the isolated Ln^{3+} layers might favor the anion conductivity through them, explaining that $LnBa_2Ca_2Fe_5O_{13}$, with a unit cell with the highest isolated Gd^{3+} layers rate in the series, also presents, in addition to the highest electronic conductivity, the best electrocatalytic properties.[30] The antiferromagnetic behavior of these Fe^{3+} containing oxides is also influenced by the ordering and type of oxygen-polyhedra around the Fe atoms, demonstrating, once again, the relationship between crystal and electronic properties.[31] Interestingly, the variation of their electrical conductivity with temperature, typical for a semiconducting mechanism, shows a smooth transition in a relatively wide range of temperatures (between ~600 K and ~900 K). The electrical transition is coupled with a broad magnetic transition, in the same temperature range, associated with the evolution of 3D into 2D-magnetic behavior.[30,31]

The studies on these complex layered perovskites are primarily focused on their physical properties in connection with their crystal structure, while the electronic structure is scarcely considered. Relatively recent advances in electronic structure theory, in particular density functional theory (DFT), in parallel with the improvements in computing power, allow explaining a great variety of materials properties and predict new compounds with certain thermodynamically stable crystal structures and behaviors. We present here a thorough computational study on the layered-perovskite $GdBa_2Ca_2Fe_5O_{13}$ (GBCFO), a potential oxygen electrode material for SOFCs. The work is focused on determining the electronic structure of the oxide to understand its functional properties and, therefore, to establish adequate relationships between its phase composition, crystal, and electronic characteristics. Among the oxides of the $A_{3m+5n}Fe_{3m+5n}O_{8m+13n}$ series, $GdBa_2Ca_2Fe_5O_{13}$ presents the highest electronic conductivity and oxygen reduction reaction activity.[30] In addition, the crystal structure of the studied oxide contains three types of oxygen-polyhedra around the Fe^{3+} cations (octahedra, tetrahedra and squared pyramids), which also seem to be associated with its superior properties. The results of the calculations also elucidate the previously observed 2D magnetic nature interplayed with the electrical behavior of the $GdBa_2Ca_2Fe_5O_{13}$, suggesting new approaches for further comprehensive experimental research in layered perovskites with 2D-behaviors.

2. Computational methods

All first-principles calculations performed in this work were executed in the VASP program package utilizing U-modified density functional theory (DFT+U).[32] The wave functions of atomic valence electrons $2s^22p^4$ for O, $3s^23p^64s^2$ for Ca, $5s^25p^66s^2$ for Ba, $3p^63d^74s^1$ for Fe and $5s^25p^66s^25d^1$ for Gd were treated with the plane augmented wave (PAW) method; the corresponding states of core electrons and atomic nuclei were evaluated with the program-supplied pseudopotentials. Some calculations implied the use of Gd pseudo-potential that included 4f-states explicitly, *i.e.* the configuration of the valence electrons for Gd atom was $5s^25p^66s^25d^14f^7$. The exchange–correlation functional used is the one proposed by Perdew–Burke–Ernzerhof (PBE) formulated within the general gradient approximation (GGA). In addition, the more recently formulated MetaGGA SCAN functional was also tested.[33] These functionals tend to give an underestimated band-gap energy while hybrid functionals more accurately deal with electron localization, in particular HSE06 ones, which are preferable for periodic solids.[34] However, hybrid functionals are computationally more expensive than semi local methods, and are also heavily dependent on the choice of the mixing parameter.[35] A common approach is the Hubbard correction that introduces a U_{eff} in the calculation of systems with strongly localized electrons of d and f types. The correction term in DFT+U was selected by following the simplified scheme proposed by Dudarev *et al.*[36] It should be stressed that the selection of the U_{eff} parameter for the 3d electronic states of Fe atoms often depends on the desired accuracy of a particular property simulation.[37] In this work, the respective value was fixed at 4.0 eV, which has previously provided correct Fe_2O_3 to Fe_3O_4 reduction enthalpies,[38] as well as reasonable electronic band gaps, crystal structure parameters and oxygen ion migration barriers for perovskite-like ferrites containing Fe^{3+} ions in octahedral, square pyramidal and tetrahedral sites.[37,39] More recently, the insulating character of the $YSr_2Cu_2FeO_7$ compound was well captured when electron correlations were treated by the GGA+U approximation using a U_{eff} value of 4.0 eV for both Fe and Cu.[40] Also, the value of U_{eff} = 4.1 eV was obtained self-consistently for Fe^{3+} cations with octahedral oxygen coordination.[41] For comparative purposes a U_{eff} value equal to 6.0 eV, calculated for lanthanides,[42] was also introduced for Gd 4f states in one of the calculations. Due to the presence of ions that possess pronounced magnetic properties (Gd, Fe) in the studied oxide, spin polarization was also considered. The cutoff energy for the plane waves was set to be 520 eV; self-consistency of the solution of Kohn–Sham equations was attained when the total energy difference between two consecutive iteration steps did not exceed 10^{-6} eV.

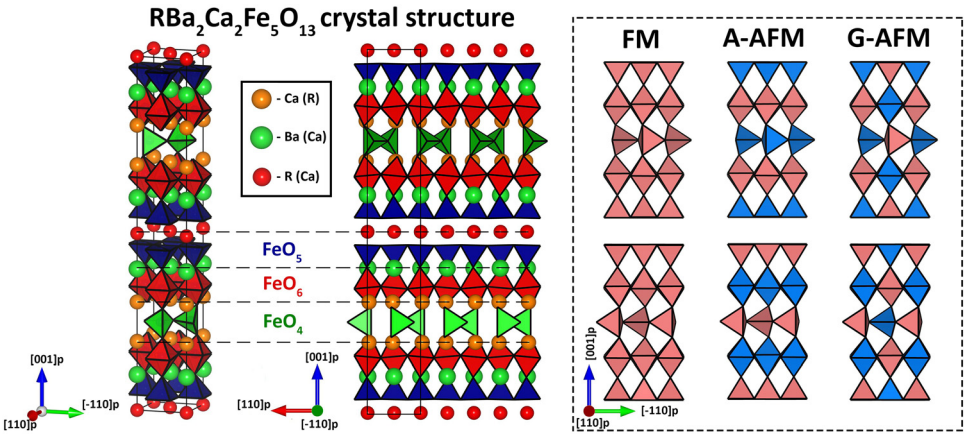

Fig. 1 Graphic representation of the $RBa_2Ca_2Fe_5O_{13}$ (R = Gd, Tb, Y) crystal structure along different projections and the corresponding magnetic orderings used in this work. Oxygen atoms are not depicted for simplicity. Instead, Fe^{3+}–oxygen polyhedra are presented; the corresponding color-coding marks the specific crystalline environment of a particular polyhedron (for the magnetic orderings the color represents the spin state of the Fe^{3+} ion located inside; light blue represents spin-down states and light red represents spin-up states). The thick black solid line shows the borders of the unit cell, horizontal dashed lines designate the structural layers under consideration. Experimentally observed defects in the ordering of the A-cation sublattice have not been contemplated in the structure.

The increased precision criterion (10^{-8} eV) was used for the calculation of the electronic spectra and related properties. All the crystal structures studied were preliminarily relaxed with respect to forces acting on every ion considered. The lattice was supposed to be converged, when the total energy difference between the two last steps of structural optimization was less than 10^{-3} eV. In addition to this, the energy-volume curve was calculated at 16 different volumes of the GBCFO unit cell; thermal dependence of the respective unit cell volume was assessed using a quasiharmonic Debye model.[43]

The crystal structure of the $GdBa_2Ca_2Fe_5O_{13}$ oxide was modelled based on the $\sqrt{2}a_p \times \sqrt{2}a_p \times 10a_p$ unit cell (a_p refers to the lattice parameter of the cubic perovskite), with orthorhombic symmetry (*Imma* space group), that contains 4 formula units and 92 atoms in total. In this work, the unit cell and atomic coordinates obtained from the structural refinement of the isostructural $TbBa_2Ca_2Fe_5O_{13}$ (TBCFO) and $Y_{0.9}Ba_{1.7}Ca_{2.4}Fe_5O_{13}$ (YBCFO) oxides using neutron diffraction data were taken as a reference.[30,31,44–47] The graphic representation of the unit cell is depicted in Fig. 1;[30] the respective unit cell directions in Fig. 1 are given in terms of the symmetry of a simple cubic perovskite lattice.[30] Three different magnetic structures (with respect to Fe^{3+} 3d electrons) were considered for the calculations (Fig. 1): one ferromagnetic (FM) and two antiferromagnetic (AFM) orderings: A-AFM and G-AFM.

To assess the thermodynamic stability of various magnetic configurations of the $GdBa_2Ca_2Fe_5O_{13}$ oxide, the total electronic energies of the Gd_2O_3, Fe_2O_3, BaO and CaO oxides were calculated. Defect formation energies in GBCFO were computed for the $2a_p \times 2a_p \times 10a_p$ supercells by utilizing the approach reported earlier.[48] Oxygen interstitials were created by introducing an additional oxygen atom in the pristine 184-atomic supercell; in turn, oxygen vacancies were made by removing one of oxygen atoms from it. The scheme of defect allocations used is provided in the SI.

Total (DOS) and partial (pDOS) density of states spectra of the $GdBa_2Ca_2Fe_5O_{13}$ oxide were computed by utilizing the Gaussian smearing method, since the unit cell parameter c is almost an order of magnitude larger compared to other typical perovskite unit cell dimensions; accordingly, the k-point sampling of the Brillouin zone (BZ) was selected to be $N \times N \times 1$, where N is a natural number. During the optimization procedure N was taken to be 4, while the electronic properties were calculated assuming $N = 8$. The band centers of mass were computed like in $BaFeO_3$.[49] Intralayer band gaps were estimated based on the position of O 2p and Fe 3d orbitals of oxygen and Fe atoms located in the different layers. Band dispersion was evaluated for the preliminarily optimized GBCFO unit cell under the constraint of preserving orthorhombic symmetry and G-AFM magnetic ordering; the distances between two adjacent high-symmetry points in BZ were interpolated by 25 k-points. Optical spectra were computed *via* a common approach reported previously.[50] The pre- and post-processing of the results was accomplished using vaspKIT software.[51] Additional calculations were made for estimating Fe–O bond strength using the LOBSTER package.[52]

To study the influence of the lattice arrangement of different FeO_x polyhedra on the electronic properties of the resulting compounds, several alternative Fe^{3+}-based crystal structures were investigated using the same GGA+U methodology as described above. Namely, orthorhombic $GdFeO_3$, tetragonal $BaCaFe_2O_5$ and hexagonal $CaBaFe_4O_8$ were utilized to represent the contribution solely from FeO_6 octahedra, FeO_5 square pyramids and FeO_4 tetrahedra, respectively. In addition, combinations of two different polyhedra (*i.e.* FeO_4 + FeO_5; FeO_4 + FeO_6 and FeO_5 + FeO_6) were assessed with the help of $NaCa_2Fe_3O_7$, $GdBaCaFe_3O_8$ and $GdBa_2Fe_3O_8$ orthorhombic crystal structures, which were based on the earlier reported structural data.[40] All of the respective calculation details are provided in the SI (Table S1 and Fig. S1).

The electronic conductivity of the $GdBa_2Ca_2Fe_5O_{13}$ compound was computed with the linearized Boltzmann's transport equation under the constant relaxation time (CRT) approximation using Boltztrap2 software.[53] The input data on band structure were obtained from the self-consistent calculation of G-AFM ordered GBCFO unit cell with the $14 \times 14 \times 2$ k-point sampling of its BZ (the partial occupancies of orbitals were determined within the tetrahedron method using Blöchl corrections[54]). The electronic conductivity tensor ($\hat{\sigma}_{CRT}$) was estimated using the following equation:

$$\hat{\sigma}_{CRT} = \frac{|\bar{e}|^2}{4k_B T}\int_0^{\infty} \Sigma_{\alpha\beta}(E)\left[\cosh\left(\frac{E-E_F}{2k_B T}\right)\right]^{-2} dE \quad (1)$$

where k_B denotes Boltzmann's constant, $\bar{e}$ is the elementary electrical charge, T is the absolute temperature, E is the energy, E_F is the Fermi level and $\Sigma_{\alpha\beta}(E)$ is the so-called transport distribution function which is determined as a sum of the integrated tensor products of electron energy derivatives over all bands considered, multiplied by the relaxation time τ:

$$\Sigma_{\alpha\beta}(E) = \frac{\tau}{8\hbar^2\pi^3}\sum_{i=1}^{N_b}\int\left(\frac{\partial E_{i\boldsymbol{k}}}{\partial k_\alpha}\right)\otimes\left(\frac{\partial E_{i\boldsymbol{k}}}{\partial k_\beta}\right)\delta_K(E-E_{i\boldsymbol{k}})d\boldsymbol{k} \quad (2)$$

with $\hbar$ denoting the reduced Planck's constant, $E_{i\boldsymbol{k}}$ the energy of i-th band at a specific $\boldsymbol{k}$ vector in the reciprocal unit cell and δ_K is the Kronecker's delta function. The summation in eqn (2) is carried out over all N_b bands in the system, while α and β indices designate two distinctive cartesian coordinates of the particular $\boldsymbol{k}$ vector. In this work the σ_{CRT} was estimated as a function of temperature and the doping level p_d; the latter one was implicitly accounted for in the actual value of the Fermi level inserted into eqn (1).

3. Results and discussion

3.1. Crystal structure and thermodynamic stability of $GdBa_2Ca_2Fe_5O_{13}$

According to the experimental data, the GBCFO oxide has a highly anisotropic orthorhombic lattice, which can be unambiguously indexed within the $\sqrt{2}a_p \times \sqrt{2}a_p \times 10a_p$ unit cell with the *Imma* space group.[30] An important feature of the synthesized $RBa_2Ca_2Fe_5O_{13}$ (R = Gd, Tb, Y) compounds is the presence of anti-site defects in the A-positions, more noticeable in the case of Y and Ca in the YBCFO.[44,46] However, *ab initio* modeling of such defect compounds implies a complicated computational approach; accordingly, certain approximations allow achieving reasonable time-to-result ratios. In this work, the A-site disordering in $GdBa_2Ca_2Fe_5O_{13}$ has been modeled by mixing Gd and Ca atoms only in their respective layers. Considering this disordering, three different 92-atomic unit cells were generated with Gd atoms substituting Ca ones and *vice versa*; the corresponding graphic representations can be found in the SI (Fig. S2). Accordingly, to assess the relative influence of A-site mixing on thermodynamic stability of the j-th structural model of the $GdBa_2Ca_2Fe_5O_{13}$ compound, the $\Delta H_{f(j)}$ enthalpy change (*i.e.* the formation enthalpy) of the following chemical reaction has been computed:

$$\frac{1}{2}Gd_2O_3 + 2BaO + 2CaO + \frac{5}{2}Fe_2O_3 \rightarrow GdBa_2Ca_2Fe_5O_{13}(j) \quad (3)$$

The term j in brackets underlines the particular structural model of the GBCFO used for the calculations. In turn, the $\Delta H_{f(j)}$ quantity can be expressed as:

$$\Delta H_{f(j)} = E^{tot}_{GdBa_2Ca_2Fe_5O_{13}(j)} - \frac{1}{2}E^{tot}_{Gd_2O_3} - 2\left(E^{tot}_{BaO} + E^{tot}_{CaO}\right) - \frac{5}{2}E^{tot}_{Fe_2O_3} + p\Delta V_j \quad (4)$$

where E_l^{tot} denotes the total electronic energy of l-th component in reaction (3), p stands for pressure and ΔV_j is the overall molar volume change in the j-th reaction (3). One should note now that the results of using formula (4) may strongly depend on the type of magnetic ordering of the GBCFO (all other oxides involved in reaction (3) are assumed to be in their most stable magnetic states at 0 K). Therefore, the calculated formation enthalpies in the framework of the GGA+U method are given in Table 1 for both structural disorder and magnetic ordering models in GBCFO. As seen, all the estimated $\Delta H_{f(j)}$ parameters are strongly negative, which indicate the thermodynamic preference of the perovskite-like structure over the mixture of binary oxides. Also, one can acknowledge that the anti-site defects in the A-sublattice of GBCFO make little difference (less than 100 meV) for the resulting $\Delta H_{f(j)}$ value; it is probable that the small energy gain observed for perfectly ordered GBCFO is counterbalanced by a higher entropy of mixing, which eventually enables the stabilization of some Ca atoms within the Gd layer in the GBCFO material. On the contrary, a much more pronounced energy difference is observed for different magnetic orderings. For instance, the calculations revealed that FM and A-AFM structures result in higher $\Delta H_{f(j)}$ values than the G-AFM ordering; the corresponding subtraction gives 1.26 and 0.78 eV per f.u. differences between G-AFM/FM and G-AFM/A-AFM configurations of perfectly ordered GBCFO, respectively. Similar results are achieved for the unit cells with the Gd/Ca mixing (models I, II and III in Table 1). One should note that these outcomes appear to be in general agreement with the Goodenough–Kanamori rules[55] and experimental observations.[31] Accordingly, the G-AFM magnetic structure is proved to be the most stable in the $GdBa_2Ca_2Fe_5O_{13}$ crystalline framework, disregarding the degree of Gd and Ca mixing; hence, further analysis will be performed only for this type of spin ordering.

Experimental data are a valuable tool for validating the results of U_{eff} corrected GGA (GGA+U) calculations. Indeed,

Table 1 The GGA+U computed formation enthalpies of the $GdBa_2Ca_2Fe_5O_{13}$ oxide with different magnetic orderings and A-site mixing models

Magnetic ordering	Formation enthalpy, eV			
	Non-mixed	Model I	Model II	Model III
G-AFM	−1.597	−1.510	−1.552	−1.520
A-AFM	−0.820	−0.729	−0.776	−0.745
FM	−0.339	−0.254	−0.291	−0.268

Table 2 Experimentally determined and DFT+U computed unit cell parameters of $GdBa_2Ca_2Fe_5O_{13}$. Experimental data were taken from elsewhere[30]

	Method		
Parameters	Experiment	GGA+U	SCAN+U
a, Å	5.5222	5.53056	5.49541
b, Å	5.5625	5.58393	5.44159
c, Å	38.309	38.106	37.375
α, deg	90	90	90
β, deg	90	89.991	90
γ, deg	90	90	90.006
V, Å^3	1176.75	1176.79	1117.66

the theoretical unit cell parameters of $GdBa_2Ca_2Fe_5O_{13}$ obtained during structural relaxation (within the G-AFM magnetic ordering) compared with those experimentally determined by X-ray diffraction in the synthesized oxide[23] are in reasonable agreement (Table 2). The very close matching of the GBCFO unit cell volumes estimated by GGA+U and Rietveld methods is especially remarkable; the respective relative difference is less than 0.01%. The computed energy-volume curve of the G-AFM ordered GBCFO additionally supports the computing results – the equilibrium volume at 0 K determined by fitting the respective points with the Birch–Murnaghan equation of state[56] is extremely close to that obtained by simple structural relaxation (see Fig. S3(a) in the SI). In addition, the extracted temperature dependence of GBCFO unit cell volume appears to be in good agreement with the experimental observations, Fig. S3(b);[57] moreover, the obtained Debye temperature ($\sim$430 K at room temperature) coincides well with the known data for similar oxide systems.[58] In contrast, the use of the SCAN functional in conjunction with the U_{eff} term (SCAN+U) brings worse results – the difference between experimental and computed unit cell volumes of GBCFO is estimated to be $\sim$5%. Therefore, one may assume that the GGA+U approximation is more precise in terms of estimating the unit cell dimensions. Hence, GGA+U approximation was used in this study.

Despite the perfect coincidence between GGA+U computed and the experimental unit cell volume of the GBCFO, the respective values of individual unit cell parameters differ significantly although the inconsistencies lie within the typical range of *ab initio* errors.[59] In addition, the structural relaxation of the GBCFO lattice has led to symmetry breaking, thus transforming the initially orthorhombic unit cell with the *Imma* space group into the monoclinic $P2_1/n$ one. The application of SCAN+U approximation has also resulted in the symmetry lowering of the GBCFO lattice, which suggests insufficient precision of structural models used in the calculations (*i.e.* one does not account for antisite-defects). However, the respective angle deviations from 90° were found to be less than 0.01 in both cases, which implies minor distortion of the GBCFO crystallographic planes.

Although estimation of unit cell dimensions is an important probing for the computational approach, it does not give information on the chemical bonds in the solid. Therefore, it is desirable to compare the calculated bond lengths with those derived from the Rietveld refinement of the structure from the corresponding diffraction data. Since these data are not available in the case of the $GdBa_2Ca_2Fe_5O_{13}$ in the literature, experimental bond lengths of the isostructural compounds $Y_{1.1}Ba_{1.6}Ca_{2.3}Fe_5O_{13}$ and $TbBa_2Ca_2Fe_5O_{13}$ will be used in this work.[31,45] The respective bond lengths and angle distributions calculated using the GGA+U method for GBCFO are given in Table 3 (the atomic coordinates obtained can be found in Table S2 in the SI). The overall agreement between the experimental bonding distances and angles, and the DFT+U computed values for the GBCFO is satisfactory. The most noticeable difference in the two datasets presented is linked with the geometry of FeO_4 tetrahedra: *ab initio* calculations predict more symmetric distribution of Fe–O bond lengths, both in the apical and equatorial positions of the oxygen-atoms. Contrary to that, experimental data of YBCFO and TBCFO show different equatorial Fe–O distances. Still, the degree of mismatch does not exceed 1% in most cases, thus suggesting an appropriate level of theoretical approximations used. In addition, it should be mentioned that the derived bulk modulus, B_0, of the GBCFO (Fig. S3(a)) agrees with the one measured for Fe^{3+} containing ferrites that simultaneously contain FeO_6 octahedra and FeO_4 tetrahedra in the structure with $\sim$1.8 Å and $\sim$2.0 Å Fe–O bond lengths respectively.[60] When only FeO_6 octahedra are present, the B_0 magnitude is usually higher.[61] Finally, it must be stated that the in-plane Fe–O–Fe bond angles for the different oxygen-polyhedra around the Fe^{3+}-cations in RBCFO are significantly

Table 3 Computed interatomic distances and in-plane bond angles for G-AFM GBCFO in comparison with the corresponding experimental data determined for the oxides containing another element R ($Y_{1.1}Ba_{1.6}Ca_{2.3}Fe_5O_{13}$ and $TbBa_2Ca_2Fe_5O_{13}$).[31,45] GGA+U derived bond lengths in different Fe^{3+}–O polyhedra were preliminarily averaged

Bond distances (Å) and angles (deg.)	Experimental		GGA+U
	R = Y	R = Tb	R = Gd
FeO_6			
d_{Fe-O} apical	2.1089	2.1332	2.1187
	2.0824	2.032	2.1187
d_{Fe-O} equatorial	1.9462	1.9559	1.9640
	1.9462	1.9559	1.9640
	1.9684	1.9667	1.9870
	1.9684	1.9667	1.9870
FeO_5			
d_{Fe-O} apical	1.8718	1.9234	1.8610
d_{Fe-O} equatorial	2.0127	1.9958	2.0201
	2.0127	1.9958	2.0201
	2.0031	1.9915	2.0170
	2.0031	1.9915	2.0170
FeO_4			
d_{Fe-O} apical	1.8686	1.7532	1.8410
	1.8686	1.7532	1.8410
d_{Fe-O} equatorial	1.8556	1.8572	1.9230
	1.9425	2.249	1.9230
d_{Fe-Fe} (R layer), Å	3.7691	3.724	3.7692
$\Theta_{Fe-O-Fe}$ (FeO_6)	168.94	166.77	171.66
$\Theta_{Fe-O-Fe}$ (FeO_5)	149.34	155.58	151.41
$\Theta_{Fe-O-Fe}$ (FeO_4)	125.06	117.88	123.96

different, which is well reproduced using the GGA+*U* method. This observation suggests that the degree of overlap between Fe-orbitals and O-orbitals differs depending on the coordination number of the Fe^{3+} cations. Hence, individual contributions from the respective 3d electronic states to DOS might vary depending on the type of Fe^{3+}–O polyhedron, as has already been reported for the YBCFO.[45]

3.2. Electronic band structure & chemical bonding of $GdBa_2Ca_2Fe_5O_{13}$

Prior to discussing the electronic structure of the studied compound, it is instructive to note that Gd is a 4f-element. Therefore, the presence of 4f-electrons might render certain influence on the resulting electron density. However, it is often assumed that in the vicinity of the Fermi level, the electronic states are essentially independent of the respective 4f-states in the rare-earth containing crystals.[62] This is also known as the frozen-core approximation.[63] With the aim to examine whether the Gd 4f electrons can indeed influence the DOS of the GBCFO, a separate calculation was made involving the previously studied $GdFeO_3$ oxide as a test compound. The actual calculations made for the G-AFM $GdFeO_3$ with and without frozen-core approximation have shown that the obtained E_g values are similar, corresponding to 2.421 and 2.412 eV respectively, see Fig. S4 in the SI. It should be noted that both results fall into the experimentally determined $GdFeO_3$ band gap range of 2.1–2.5 eV;[64] moreover, they are almost indistinguishable from each other. In addition, the computed distribution of Fe and O electronic states within the bands for both approaches used appears to be the same in the vicinity of the Fermi level (Fig. S4). The obtained result is reasonable, as the corresponding Gd 4f states were found to lie ~5.5 eV beneath the top of the valence band (VB), (Fig. S4); accordingly, their influence on the Fe and/or O states should be insignificant. The reported numerical estimations of magnetic interactions fully support this conclusion.[64] Hence, the frozen core approximation can be accurately utilized for treating the electronic structure of the GBCFO oxide.

The computed DOS spectrum under the GGA+*U* approximation of the GBCFO oxide is presented in Fig. 2(a). The results indicate that the studied compound is a narrow-gap semiconductor with a band gap value of E_g = 0.53 eV. The corresponding estimation of partial contributions to DOS reveal typical particularities for Fe^{3+} containing perovskites – the severely spin-split Fe 3d band, part of which is forming the bottom of the conduction band (CB) and a wide O 2p band providing the top of the VB.[64–67] One can also acknowledge the overlying Gd 4d states (~4 eV above the bottom of the CB) which are too high in energy to participate in the electron conduction process. Accordingly, the electronic structure of the GBCFO, in general, represents the common picture of localized electrons in a transition metal oxide.[49]

However, the implication of the layered crystalline architecture causes some peculiarities to appear in the DOS spectrum. Namely, the distribution of electronic states for Fe and O atoms was shown to depend on the Fe^{3+}-environment in the unit cell, in particular on the exact type of oxygen-polyhedron around the Fe^{3+} cations. The mentioned data are shown in more detail in

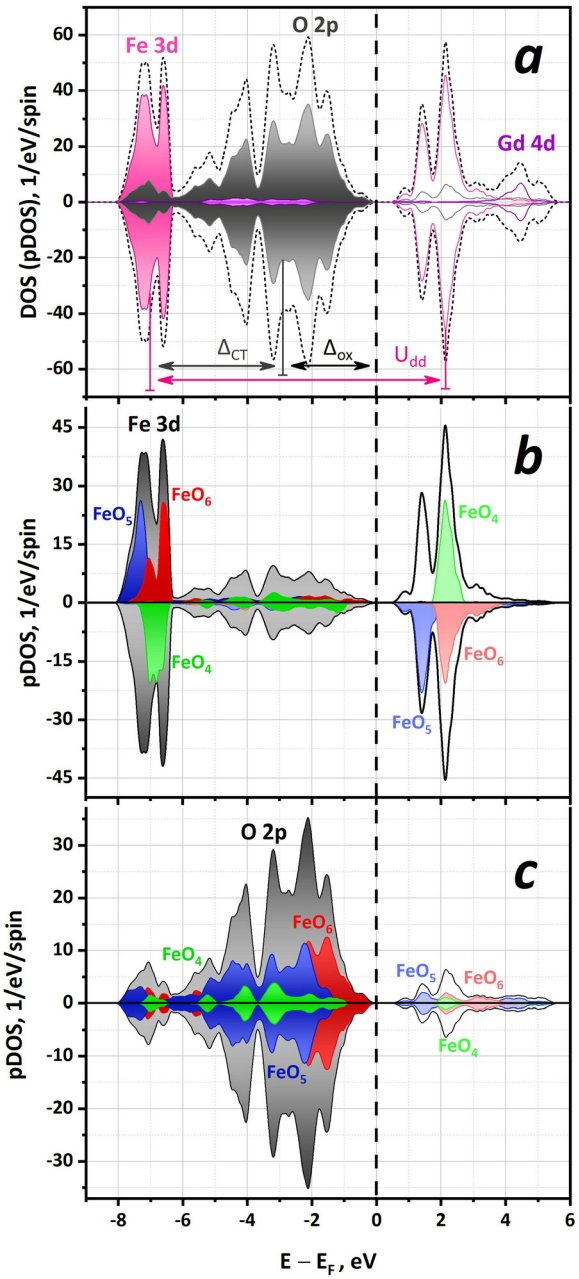

Fig. 2 The GGA+*U* computed electronic spectra of $GdBa_2Ca_2Fe_5O_{13}$. (a) The total DOS (dotted line) and pDOS (filled areas/solid lines) curves evaluated for all Gd, Fe and O atoms in GBCFO (filled areas show filled states, solid lines above the Fermi level designate empty states). (b) pDOS of the Fe-sublattice in GBFCO (filled grey area/black solid line) and respective partial contributions from Fe^{3+} cations located in different oxygen polyhedra (filled colored areas); lighter colors correspond to empty states. (c) pDOS of the O-sublattice (filled grey area/black solid line) and respective partial contributions from oxygen ions located in layers belonging to different oxygen polyhedra around the Fe^{3+} ions (filled colored areas); non-colored areas correspond to empty states. Negative values designate spin down states. The vertical dashed line shows the position of the Fermi level. The type of polyhedron associated with a certain pDOS, is also marked on the figure.

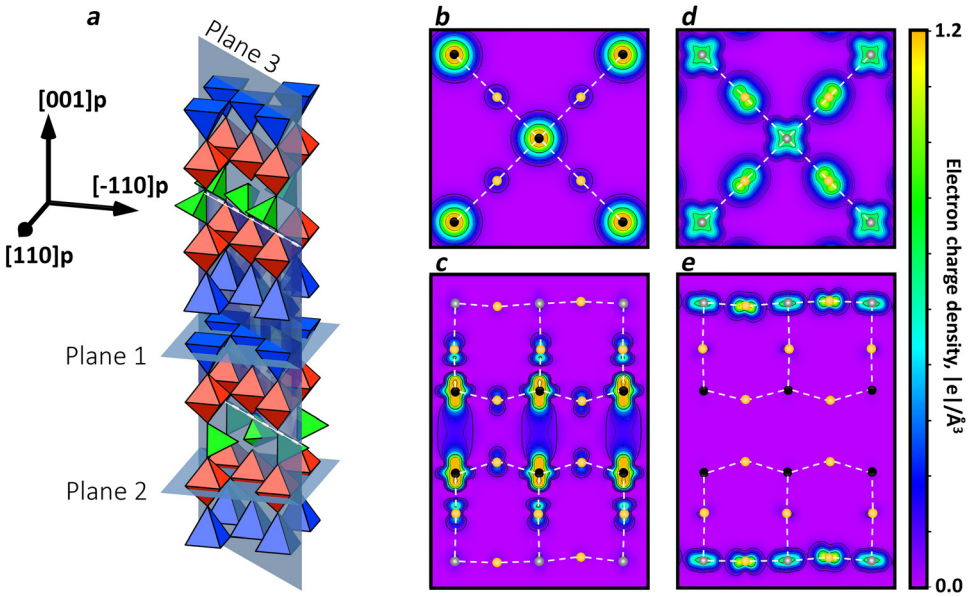

Fig. 3 Graphical representation of the crystal structure of $GdBa_2Ca_2Fe_5O_{13}$ (a); the corresponding representation omits the A-site cations and oxygen anions for simplicity – only oxygen polyhedra around Fe^{3+} cations are shown. The GGA+*U* computed charge densities of electrons in the conduction, (b) and (c), and valence, (d) and (e), bands of GBCFO are shown, projected onto specific crystallographic planes. The respective planes are schematically shown in panel (a) as rectangles that cross-section the unit cell of GBCFO. Panel (b) corresponds to the charge density projected onto plane 1, panel (c) to that projected onto plane 3, and panel (d) to that projected onto plane 2. Panel (e) represents the electron density projected onto plane 3. Panels (c) and (e) show the charge density projections along the $[001]_p$ direction; the respective span range is marked on plane 3 by white solid lines (a). The presented charge density maps (b, c, d and e) also contain the positions of Fe atoms resting in FeO_6 octahedra (shown as grey spheres) and in FeO_5 pyramids (shown as black spheres). Oxygen sites are also marked as bright yellow spheres along with the respective Fe–O bonds (dashed white lines).

Fig. 2(b) and (c) for Fe 3d and O 2p states, respectively. Considering the information presented in Fig. 2(b) one can notice the wide low-intensity Fe band ranging from −6 eV up to the Fermi level; these are the Fe 3d–O 2p hybridized states. At the same time, peak-shaped Fe 3d states located both in the VB and in the CB are split with the lower energy peak corresponding to pyramidally coordinated Fe atoms. In turn, higher energy states are provided by a combination of electrons bound to the Fe atoms located in the FeO_4 tetrahedra and FeO_6 octahedra. Given the large splitting energy (>1 eV), it is concluded that the FeO_5 layers are mainly responsible for the formation of the CB in GBCFO. On the other hand, the pDOS of the O 2p states in equatorial oxygen positions of the different polyhedron (*i.e.* FeO_4 tetrahedron, FeO_5 square pyramid or FeO_6 octahedron) shows that the top of the VB is also spatially specific (Fig. 2(c)). Namely, only those states that belong to equatorial oxygen atoms located in FeO_6 octahedra do contribute to the top of the VB. The states of oxygen ions in FeO_4 and FeO_5 polyhedra appear to be ∼1 eV lower in energy and hence their influence on electrical transport properties can be neglected. Accordingly, GBCFO may be considered as a 2D-semiconductor with FeO_5-layers acting as the CB, FeO_6-layers as the VB and FeO_4 ones as effectively insulating channels. This result seems to be controversial, as a previous report in the isostructural YBCFO suggested the top of VB is in the FeO_4-layer.[45] Still, the use of other functionals (*i.e.* SCAN) in this work gives similar distribution of the electronic states.

It is important to notice that the computed band gap value (0.53 eV) for the GBCFO is unusually small in comparison with the other Fe^{3+}-perovskites.[60,68,69] Considering the relationship between electric bandgap and optical bandgap, we have calculated the optical spectrum of the G-AFM GBCFO, see Fig. S5 in the SI. The color of the solid can be estimated theoretically from its reflectance spectrum.[70] The one of the GBCFO (Fig. S5) shows that its reflectance is approximately constant in the visible range; the respectively estimated CIE-color[71] is dark brown in agreement with the experimental color of the studied oxide,[30] although the determined band gap suggests the material should be totally black.[70] This counterintuitive result originates from the peculiar band dispersion in GBCFO – the calculated energy band diagram (Fig. S6 in the SI) indicates that the band gap in the studied compound is indirect in nature and hence the relative contribution of the electronic transition to the overall light absorption should be small. In contrast, the strongest impact on optical absorption is provided by direct transitions, which are higher in energy (above 2 eV). Consequently, the intense increase of optical absorbance in GBCFO is observed only at UV wavelengths, which explains the non-black color of the material considered.

Although the DOS spectra provide important information about the electronic structure, they do not allow to estimate the spatial localization of bands, which is of special importance for semiconductors. Fig. 3 displays the calculated electron charge densities in the CB and VB projected onto specific crystallographic planes of the GBCFO structure. The spatial

distribution of charge within the CB and VB is significantly different. The charge distribution in the CB is revealed to be essentially localized on Fe atoms located in the FeO_5 square pyramids, while in the VB the charge is more delocalized with comparable contributions of the Fe atoms and equatorial oxygens of the FeO_6 octahedra. These findings fully coincide with the conclusions derived from the DOS/pDOS spectra (Fig. 2). Importantly, both bands show pronounced anisotropy of the charge distribution – they appear to be concentrated mainly in the quasi-2D layers perpendicular to the *c*-axis ($[001]_p$ direction), see Fig. S7 in the SI, in agreement with the evaluated band dispersions (Fig. S6). The analysis of different projections of charge density in the CB, Fig. 3(b) and (c), indicates the conducting states are mainly formed by $d_{3z^2-r^2}$ Fe orbitals. The VB shows the Fe 3d–O 2p hybridized behavior of the $d_{x^2-y^2}$ Fe states, Fig. 3(d) and (e). It should be stated that the derived picture of charge distribution in conjunction with the observed band curvatures (Fig. S6) suggests that the electronic transport in the CB should be more localized than in the VB in agreement with earlier studies in other Fe^{3+}-perovskites.[37,72,73]

The unique coexistence of the three different types of Fe^{3+}-environment in the crystal structure makes the RBCFO (R = Y, Gd, Tb) oxides an interesting playground for testing the influence of the oxygen coordination of Fe^{3+} cations on their complete electronic behavior. In this sense, the NPD experiments on TBCFO revealed different magnetic moments localized on Fe^{3+} ions (μ_{Fe}) depending on their oxygen coordination.[31] The calculated data for GBCFO and the experimental values determined for TBCFO are compared in Table 4. Regarding the individual magnetic moments, GGA+*U* calculations give correct (within the 6% error limit) values for Fe atoms located in the FeO_5 square pyramids and FeO_6 octahedra but fail to predict the significant decrease of the μ_{Fe} in FeO_4 tetrahedra. It is important to notice that a similar issue was detected for the $Ca_2Fe_2O_5$ brownmillerite where the experimentally observed difference between the μ_{Fe} in FeO_4 and FeO_6 polyhedra[74] was not properly reproduced by DFT+*U* calculations.[66] Nevertheless, the detailed analysis of the pDOS spectra of GBCFO has shown that the electronic states in FeO_4 layers do not contribute to VB and CB edges and hence the improper μ_{Fe} values cannot be considered as substantial incorrectness of the calculation method.

As follows from the data presented in Table 4, the partial E_g values are significantly higher (if compared to the total E_g) for each polyhedron type but E_g is especially large in the case of the FeO_4 tetrahedra ($\sim$2.8 eV), assuming these sites form insulating layers in the GBCFO lattice. Notably, a very close band gap is obtained for $CaBaFe_4O_8$ that contains entirely FeO_4 structural units in its lattice, see Fig. S8(a); this result is also supported by the respective optical measurements (Fig. S8(b)). In addition, the computed E_g values for $GdFeO_3$ and $BaCaFe_2O_5$ oxides (Fig. S9 in the SI) that contain only FeO_6 and FeO_5 structural units respectively, were found to be in qualitative coincidence with the data obtained for individual FeO_6 and FeO_5 layers in GBCFO, see Table 4. Considering all the above results, one can suppose that the combination of FeO_4, FeO_5 and FeO_6 polyhedra in one lattice provides a synergetic effect on the resulting electronic band structure.

To support this conclusion, it is important to study the implications in the band structure due to the elimination of one of the types of the FeO_x polyhedra. In this context, another compound of the $A_{3m+5n}Fe_{3m+5n}O_{8m+13n}$ series was considered, the $Gd_{1.2}Ba_{1.2}Ca_{0.6}Fe_3O_8$, which contains only FeO_4 tetrahedra and FeO_6 octahedra.[30] The calculation was made for the perfectly ordered $GdBaCaFe_3O_8$. The GGA+*U* computed DOS/pDOS spectra for the $GdBaCaFe_3O_8$ oxide are presented in Fig. 4(a) (the corresponding representation of the unit cell is given in the inset[30]). In this case, the Fe-3d levels in the CB and the VB show similar positioning on the energy scale, disregarding the actual FeO_x polyhedron type, which differs from the spectrum of the $GdBa_2Ca_2Fe_5O_{13}$. In addition, the band gap of $GdBaCaFe_3O_8$ is estimated to be $\sim$2.2 eV, thus falling in the typical range of E_g values of Fe^{3+}-perovskites.[68,69]

Another possibility is the combination of either FeO_5 square pyramids and FeO_6 polyhedra, or FeO_5 pyramids and FeO_4 tetrahedra. These combinations containing only Fe^{3+} ions can be modeled by $GdBa_2Fe_3O_8$ and $NaCa_2Fe_3O_7$ structures, respectively. Although such compounds have not been reported experimentally, the corresponding unit cells were built based on the known structures of $YSr_2Cu_2FeO_8$ and $YSr_2Cu_2FeO_7$,[40] which resemble in a certain sense the GBCFO lattice. The computed DOS/pDOS spectra of $GdBa_2Fe_3O_8$ and $NaCa_2Fe_3O_7$ are presented in Fig. 4(b) and (c), respectively. As shown, the copresence of FeO_6 and FeO_5 polyhedra results in the lowest band gap of $\sim$1.1 eV; importantly, this result corroborates with the noticeable splitting of Fe 3d states in the CB of $GdBa_2Fe_3O_8$ among the respective polyhedra, Fig. 4(b). In turn, the combination of FeO_4 tetrahedra and FeO_5 pyramids provides a band gap of $\sim$1.6 eV, Fig. 4(c), which is in between of E_g values obtained for $GdBa_2Fe_3O_8$ and $GdBaCaFe_3O_8$. Interestingly, bringing two different types of FeO_x polyhedra in one lattice allows for certain E_g reduction, if compared to the case of crystals that have only octahedra (E_g = 2.41 eV), only square pyramids (E_g = 1.35 eV) or only tetrahedra (E_g = 3.02 eV). Still, none of the double combinations provide as much band gap contraction as is observed in the GBCFO case. Therefore, it

Table 4 Calculated electronic parameters of the GBCFO oxide. U_{dd} is the magnitude of splitting of the Fe 3d states, Δ_{CT} is the charge transfer energy, and Δ_{ox} is the average amount of energy required to transfer electron from the O-2p band to the top of the VB. The presented data are associated to the oxygen environment of the Fe atoms. The numbers in brackets in the top row represent the experimental values obtained for TBCFO[24]

Parameters (eV)	Crystallographic environment			
	Tot	FeO_6	FeO_5	FeO_4
$\lvert\mu_{Fe}\rvert$, μ_B	0.0 (0.0)	4.09 (3.9)	4.04 (3.8)	4.05 (3.0)
E_g	0.53 (0.38[a])	1.90 (2.4[b])	1.67 (1.35[b])	2.79 (3.02[b])
U_{dd}	+9.05	+9.16	+8.7	+9.05
Δ_{CT}	−4.08	−3.83	−3.73	−3.63
Δ_{ox}	+2.93	+2.93	+3.41	+3.23

[a] The value is estimated from the temperature dependence of the GBCFO conductivity.[23] [b] The band gaps are obtained for the compounds with only one type of FeO_x polyhedron.

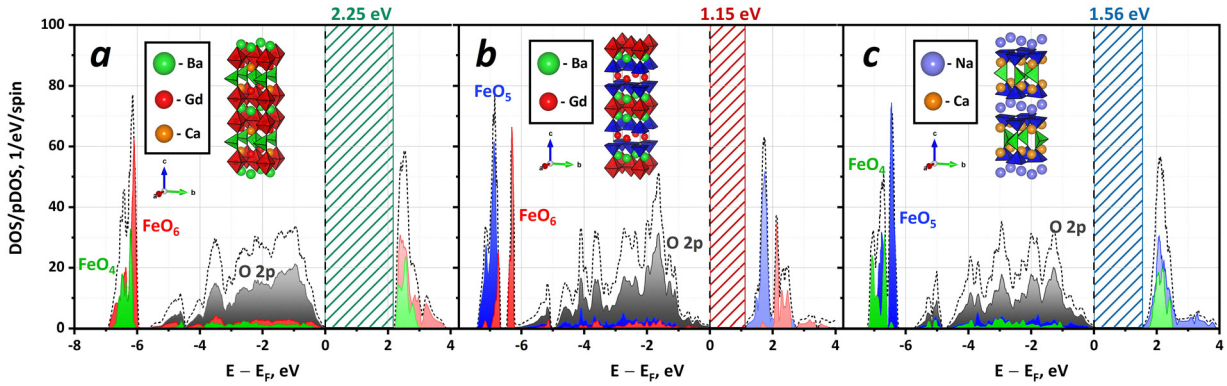

Fig. 4 DOS spectra (dashed lines) of $GdBaCaFe_3O_8$ (a), $GdBa_2Fe_3O_8$ (b) and $NaCa_2Fe_3O_7$ (c) oxides calculated using the GGA+*U* method. Colored areas depict the pDOS of Fe 3d states computed for Fe atoms located in octahedra (red color), square pyramids (blue color) and tetrahedra (green color). The spin-down states are not shown as they are fully symmetrical to the spin-up ones. The vertical dashed lines show the position of the Fermi level. The insets depict graphic representations of the crystal structures of the respective compounds. The hatched rectangles show the width of the estimated band gap; the respective numerical values are also provided for each panel.

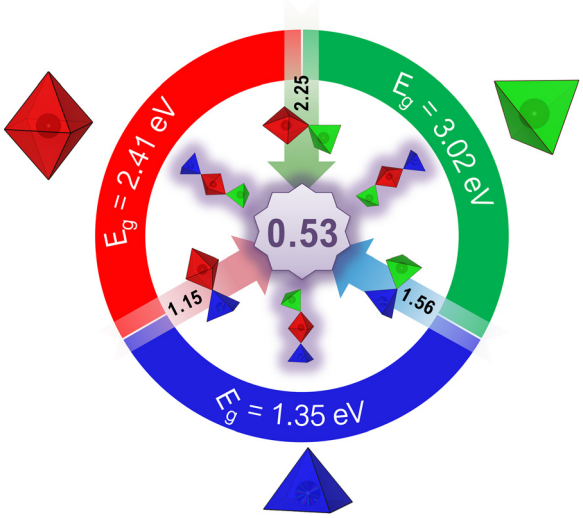

Fig. 5 Graphic representation of the influence of different combinations of FeO_x polyhedra on the band gap of perovskite-related lattices.

seems that the co-presence of all three FeO_x structural units discussed is indeed required to obtain a narrow band gap in Fe^{3+} containing perovskite-like compounds. The schematical depiction of the observed peculiarity is shown in Fig. 5.

The obtained DOS of GBCFO (Fig. 2) allows us to elucidate other important band structure parameters, also collected in Table 4: U_{dd}, the magnitude of splitting of the Fe 3d states; Δ_{CT}, the so-called charge transfer energy; and Δ_{ox}, the average amount of energy required to transfer electrons from the O-2p band to the top of the VB.[49] The magnitude of these parameters is schematically shown in Fig. 2(a). Determination of the respective band centers, which can be done using multiple ways, must be carried out to compute U_{dd}, Δ_{CT} and Δ_{ox}. In this work, it was assumed that the band center of the Fe-related states should not include those located in a wide Fe 3d–O 2p hybridized band; in turn, a similar approach was utilized for the O-2p states that contribute to Fe-3d peaks placed deep in the VB and CB. The calculated values suggest that the studied compound is a negative charge transfer oxide, which is characteristic of Fe^{3+}-perovskite-type oxides.[49] The high magnitude of U_{dd} energy (>9 eV) provides strong evidence that under oxidation of GBCFO, the increased charge will be accumulated on oxygen sites.[47] In turn, the large Δ_{ox} parameter (~3 eV) implies high energy required for oxygen vacancy formation in GBCFO, which is indeed experimentally observed.[30,44] Therefore, one can acknowledge the sufficient precision of GGA+*U* approximation utilized in this work, capable of reproducing the key experimental findings reported previously.

Considering the essential differences in the computed pDOS spectra between the alternating layers with different Fe-environments in GBCFO, individual estimation of U_{dd}, Δ_{CT} and Δ_{ox} for these layers makes certain sense. The respective data for FeO_4-, FeO_5- and FeO_6-containing layers are given in Table 4 (importantly, the discussed estimation of band structure parameters did not involve apical oxygen sites but only equatorial ones). The charge transfer energy remains essentially the same disregarding the polyhedron type, which means that the electrons transferred from any Fe site in GBCFO will be immediately replaced (with approximately the same speed) by other electrons from the O-2p formed VB. However, the magnitude of the U_{dd} energy is slightly lower for the Fe atoms in the FeO_5 square pyramids. Apparently, this observation may be responsible for the revealed particularity of CB formation in the GBCFO. In accord with that, the lowest Δ_{ox} value is calculated for FeO_6-containing layers, thus explaining why these d-orbitals form the top of the VB.

A certain alignment with the previously discussed data can be found in the LOBSTER computed partial Crystal Orbital Hamilton Population (pCOHP) curves, which basically show the bonding (if pCOHP < 0), non-bonding (pCOHP = 0) or anti-bonding (when pCOHP > 0) characteristic of the chemical interactions.[52] The respectively estimated pCOHP curves for the

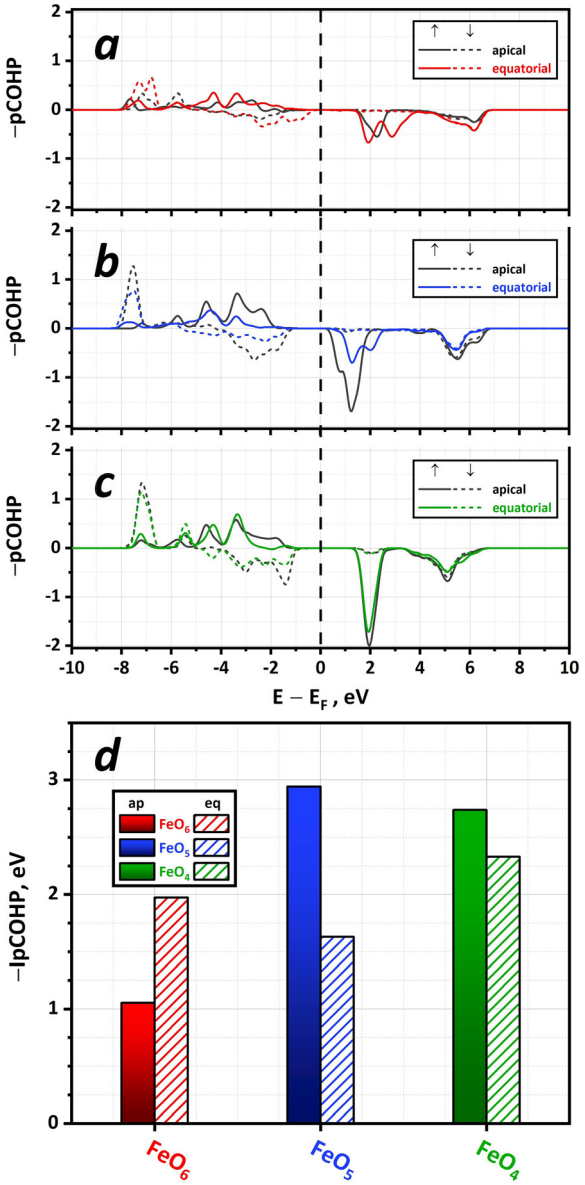

Fig. 6 The LOBSTER computed pCOHP curves for Fe–O bonds in FeO_6 octahedra (a), FeO_5 square pyramids (b) and FeO_4 tetrahedra (c) of GBCFO. Solid lines show spin-up contributions and dotted lines spin-down ones. Colored lines correspond to Fe–O bonding of oxygen in equatorial sites. The Fermi level position is marked with a vertical dashed line. The respectively obtained IpCOHP values are presented in panel (d). The data on both spin channels were summed up for each bar. Filled bars show IpCOHP between apical oxygens and Fe, the hatched ones depict IpCOHP between equatorial oxygens and Fe atoms.

Fe–O bonds in the different oxygen coordination polyhedra of GBCFO lattice are shown in Fig. 6. The results indicate that chemical interaction between Fe and oxygen atoms exhibits a strong bonding characteristic deep in the VB (<-6 eV) disregarding the type of polyhedron, apical or equatorial allocation of the oxygen ions and Fe^{3+} spin state. This conclusion agrees with previous findings in $BaFeO_3$.[49] Similarly, pCOHP values become positive in the CB of the GBCFO for all considered cases, which marks the anti-bonding characteristic of the interactions and hence the excited nature of these states. Interestingly, the bonding type between Fe-3d and O-2p electrons in the upper part of the VB (*i.e.* in the energy range from −6 to 0 eV) is found to be spin-dependent: spin-up electrons of Fe atoms form bonding type interactions, while the inverse process is observed for spin-down electrons. As discussed previously,[49] this observation comes from the inversion of the respective contributions of 3d and 2p orbitals to the Fe–O chemical bond depending on the spin state of the 3d electrons. In this sense, the type of oxygen polyhedron around the Fe atoms should not change that picture, which is indeed observed in the case of GBCFO. However, the shape and relative position on the energy scale of a certain pCOHP are shown to be highly dependent on the Fe-coordination. For instance, the anti-bonding Fe–O states in the CB, that belong to FeO_5 square pyramids are located much closer to the Fermi level in comparison with the FeO_4 or FeO_6 cases (Fig. 6(b)). The anti-bonding interactions between Fe and O atoms observed at the top of the VB correspond to the FeO_6 octahedra (Fig. 6(a)). Finally, in the case of FeO_4 tetrahedra, the characteristic of chemical interaction appears to be non-bonding in the vicinity of the Fermi level. All the above results suggest that the excited electronic states in the GBCFO tend to localize either in FeO_5 layers (when considering electrons in the CB) or in FeO_6 ones (when implying electron holes in VB). At the same time, those states located in FeO_4 layers can be considered as effectively insulating (Fig. 6(c)) in complete agreement with the conclusions derived from the DOS data.

Essential information about the chemical bond strength can be obtained by the integration up to the Fermi level of the pCOHP curves (IpCOHP). These data quantitatively measure the energy of covalent bonds in eV units;[52] it can often be used as a guideline for searching the most probable defect configurations in non-stoichiometric oxides.[49,75] The respective results for Fe–O bonds in GBCFO are presented in Fig. 6(d). All computed IpCOHP values are negative, which marks the essential chemical stability of Fe^{3+}-perovskites. However, the magnitude of |IpCOHP| differs drastically depending on the Fe-coordination. In particular, the magnitude of IpCOHP for the apical oxygens and Fe atoms located in FeO_6 octahedra indicates low bond strength. Contrary to that, in the case of other FeO_x polyhedra, the respective quantity significantly increases, thus suggesting that apical oxygen ions are much more strongly bonded to FeO_4 tetrahedra and FeO_5 square pyramids. It should be noted that this conclusion nicely coincides with the GBCFO bond lengths presented in Table 3 – the shorter the bond, the stronger the bonding and *vice versa*. Accordingly, one can expect that apical oxygen sites of the FeO_5-units are unlikely to become vacant. In contrast, the equatorial positions have other distribution of IpCOHP energies with the highest one belonging to Fe–O bonds located in FeO_5 square pyramids, suggesting that these positions are the most probable sites for oxygen vacancy formation. However, one should consider that the largest (among other polyhedra) Δ_{ox} value in FeO_5 (see Table 4) implies higher energies to transfer electrons from the hybridized Fe 3d–O 2p band to

the Fermi level. Hence, one may expect the decreased |IpCOHP| value in the case of FeO_5 pyramids as evidence of Fe–O bond extension induced by the absence of apical oxygen atoms in the Gd layer. Accordingly, the most probable place for oxygen vacancy formation in GBCFO is the equatorial O sites in FeO_6 octahedra.

3.3. Electronic conduction behavior of $GdBa_2Ca_2Fe_5O_{13}$

The studied compound has a crystal structure that induces a highly anisotropic magnetic behavior.[24] In this sense, the band structure of the GBCFO reveals pronounced 2D character of the electronic states' distribution. This result implies that the electronic conductivity of the GBCFO should be dependent on the direction of the applied electric field propagation. Taking into account that the crystalline lattice of GBCFO has orthorhombic symmetry, and considering the crystallographic directions of the cubic perovskite structure, one can write its electronic conductivity tensor $\hat{\sigma}_{el}$ as:

$$\hat{\sigma}_{el} = \begin{bmatrix} \sigma_{el}\|[110]_p & 0 & 0 \\ 0 & \sigma_{el}\|[-110]_p & 0 \\ 0 & 0 & \sigma_{el}\|[110]_p \end{bmatrix} \quad (5)$$

where $\sigma_{el}\|[110]_p$, $\sigma_{el}\|[-110]_p$ and $\sigma_{el}\|[001]_p$ denote individual contributions, being parallel to the $[110]_p$, $[-110]_p$ and $[001]_p$ crystallographic directions respectively (see Fig. 1 for more details). Eqn (5) suggests that by measuring conductivity in different directions of a GBCFO single crystal, the exact values of each $\hat{\sigma}_{el}$ tensor component can be determined. However, the available experimental data correspond to a polycrystalline sample, which makes a direct comparison with eqn (5) difficult. To overcome this problem one can assume that the GBCFO grains are small enough to be randomly oriented in the sample studied. Then, the experimental conductivity σ_{exp} can be expressed as a normalized trace of $\hat{\sigma}_{el}$ which yields the following simple result:

$$\sigma_{exp} = \langle\hat{\sigma}_{el}\rangle = \frac{\sigma_{el}\|[110]_p + \sigma_{el}\|[-110]_p + \sigma_{el}\|[001]_p}{3} \quad (6)$$

where angular brackets denote the averaging procedure. Accordingly, direct comparison between computed $\langle\hat{\sigma}_{CRT}\rangle$ and measured σ_{exp}[30] becomes possible; the respective data are given in Fig. 7(a). It is worth mentioning that the CRT approach used in this work does not allow us to properly estimate the magnitude of relaxation time τ. However, the previously published results suggest this parameter lies within the range of few dozens of femtoseconds (10^{-15} s).[76] Therefore, one can assume τ = 10 fs for the GBCFO, which agrees with the independently evaluated τ for the donor-doped $SrTiO_3$ perovskite.[73]

Prior to discussing the peculiarities of transport phenomena in the studied material it is instructive to provide a brief description of its defect structure; the respective information allows to elucidate the concentration of charge carriers in the VB and CB, which is of primary importance for electronic conductivity calculations. Given that GBCFO is a narrow band-gap semiconductor it is necessary to account for different extrinsic processes of defect formation, as well as for the intrinsic thermal ionization. For instance, one can suppose that oxygen incorporation can occur into the different structural vacancies in the GBCFO lattice, *i.e.* into FeO_5 or FeO_4 layers, thus producing interstitial sites O_i. Another possibility is that oxygen vacancies V_O can be formed – these can be located in all FeO_x polyhedra. The list of possible sites for hosting defects, as well as the corresponding defect formation reactions are given in the SI. The results of GGA+U calculations of the j-th defect formation enthalpies $\Delta H_{df}(j)$ in GBCFO oxide are presented in Table 5.

As can be seen, oxygen vacancies are very unlikely to form with the respective enthalpies computed to be higher than 3 eV. Still, these results align well with the experimental data[77] and can be explained by high energy penalties to convert Fe^{3+} into

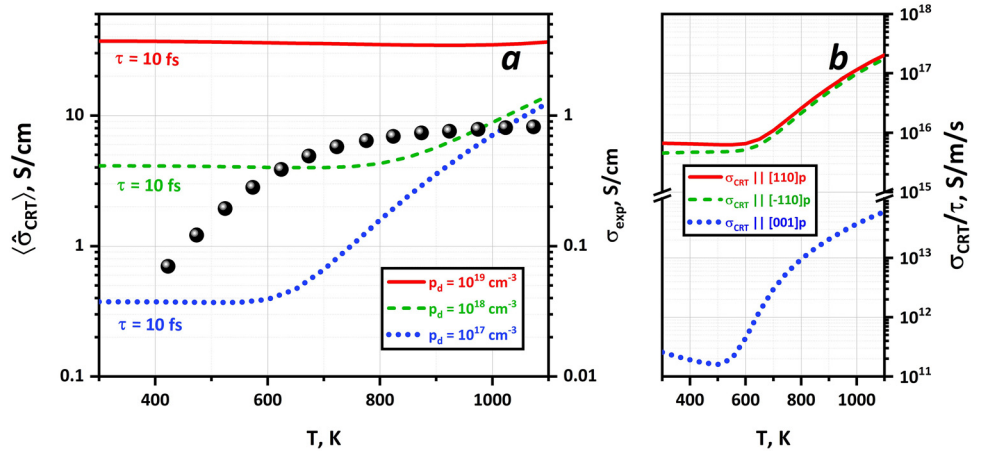

Fig. 7 The calculated (lines) and experimentally measured (points) electronic conductivities of polycrystalline GBCFO *vs.* temperature (a). The numerical values of $\langle\hat{\sigma}_{CRT}\rangle$ are obtained assuming τ = 10 fs; the influence of different doping level p_d is also accounted for. Theoretically computed σ_{CRT}/τ functions being parallel to different directions of GBCFO lattice *vs.* temperature (b). The doping level for each curve is taken to be $p_d = 10^{17}$ cm^{-3}.

Table 5 Defect formation enthalpies in GBCFO oxide as obtained from GGA+U calculations

Defect formation process		$\Delta H_{df}(j)$, eV
V_O formation	FeO_6	3.057
	FeO_5	3.287
	FeO_4	3.253
O_i formation	FeO_5	0.654
	FeO_4	1.202

Fe^{2+} in perovskite-oxides. In addition, the predicted trend of FeO_6 octahedra to the sites which are most susceptible to hosting vacancies (the Δ_{ox} parameter was found to be the lowest for FeO_6 polyhedra, see Table 4) seems to be supported by actual calculations, Table 5. On the other hand, the formation of interstitial oxygen appears to be intricated, although the relative fraction of O_i defects (especially of those formed in FeO_5 layers) will be higher than that of oxygen vacancies under oxidative conditions (*i.e.* in air atmosphere). Still, as follows from the calculated results, the overall deviation of oxygen content in $GdBa_2Ca_2Fe_5O_{13\pm\delta}$ from 13 should be small ($|\delta|$ will be less than 0.01 at 1000 K and under an air atmosphere). The available thermogravimetric data support this conclusion – the measured mass change of GBCFO when heating in air was found to be negligible.[57] What is even more interesting is that the positive sign of ΔH_{df} of the O_i formation process implies that the fraction of interstitial oxygen will increase with temperature. Accordingly, the number of holes in the VB will grow with heating. Given that $\Delta H_{df}(O_i) < \Delta H_{df}(V_O)$ and $\Delta H_{df}(O_i) > 0$, one can reasonably assume electron holes will be the main charge carriers in GBCFO under SOFC cathode conditions.

In agreement with the conclusions of the previous paragraph, the determination of the $\langle\hat{\sigma}_{CRT}\rangle$ value was made assuming acceptor doping level (p_d) to be of 10^{17}–10^{19} cm^{-3} in magnitude, which roughly corresponds to $\delta \in [-10^{-5}, -10^{-3}]$ per $GdBa_2Ca_2Fe_5O_{13}$ formula unit. The estimated conductivity curves at $p_d < 10^{18}$ cm^{-3} are shown in Fig. 7(a) and reveal the transition from the extrinsic to the intrinsic regime as the temperature increases. One can acknowledge the obtained $\langle\hat{\sigma}_{CRT}\rangle$ numerical values at $p_d = 10^{17}$ cm^{-3} are close to those (σ_{exp}) measured in the experiment. Notably, when the doping amount is higher (*i.e.* $p_d = 10^{19}$ cm^{-3}), the shape of the conductivity plot becomes almost temperature independent. These results are in agreement with the experimental findings. Indeed, defect formation enthalpies suggest that the concentration of holes should increase with temperature, *i.e.* $p_d = f(T)$. And hence, the experimentally observed $\sigma = f(T)$ of GBCFO originates from the intrinsic regime at low temperatures (due to the narrow band gap) and hole-doped regime, which is invoked by the incorporation of interstitial oxygen into the crystal lattice, at higher temperatures. Importantly, this mechanism qualitatively explains the flattening of the $\sigma_{exp} = f(T)$ curve at $T > 800$ K, see Fig. 7(a).

Accounting for the discussed crystalline anisotropy of GBCFO it is interesting to consider the direction-dependent components of $\langle\hat{\sigma}_{CRT}\rangle$. The respective data represented as σ_{CRT}/τ functions are given in Fig. 7(b). Those components of conductivity tensor that are parallel to either $[110]_p$ or $[-110]_p$ crystallographic directions (*i.e.* planes (001), also named planes *ab*) are 3–4 orders of magnitude higher than those parallel to the $[001]_p$ direction. In addition, the $\sigma_{CRT}\|[110]_p$ and $\sigma_{CRT}\|[-110]_p$ values are almost similar. Therefore, both magnitudes will be referred to as $\sigma_{CRT}(\|)$, while the quantity $\sigma_{CRT}\|[001]_p$ will be designated as $\sigma_{CRT}(\perp)$. This denomination underlines that the obtained result shows direct evidence of the anisotropy of the GBCFO electrical properties. However, the reason behind the uncovered phenomenon seems to be unclear. In this sense, the previous computational study for the YBCFO suggested that the absence of oxygen ions in the Y layer provided the main contribution to the 2D characteristic of electronic conduction.[44] In turn, the present study provides a more complicated picture where all polyhedral layers in the GBCFO lattice play a certain role in providing the anisotropic behavior. But indeed, the elimination of the FeO_5 square pyramids should result in a more isotropic $\langle\hat{\sigma}_{CRT}\rangle$; the respective evaluations made for $GdBaCaFe_3O_8$ and presented as a ratio between $\sigma_{CRT}(\|)$ and $\sigma_{CRT}(\perp)$ components of conductivity tensor clearly confirm this statement, see Fig. 8. In fact, the corresponding pDOS data suggest that the CB of $GdBaCaFe_3O_8$ is composed from electronic states of both FeO_6 and FeO_4 structural units (Fig. 4(a)). Therefore, it can be deduced that in the case of the acceptor doped GBCFO the main reason for the anisotropic behavior of $\langle\hat{\sigma}_{CRT}\rangle$ is the combination of FeO_6 layers forming the top of the VB and the large slabs composed of FeO_{65} and FeO_4 polyhedra that provide effective isolation of the

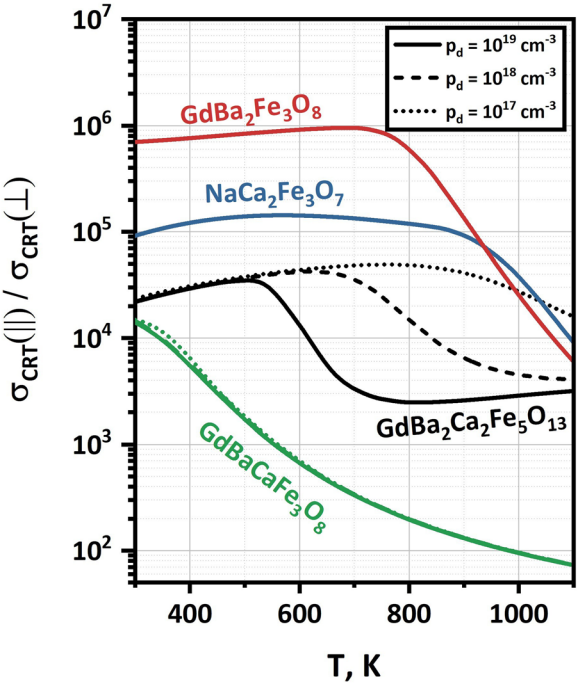

Fig. 8 The ratio of $\sigma_{CRT}(\|)$ to $\sigma_{CRT}(\perp)$ components of the conductivity tensor as a function of temperature and acceptor doping level calculated for different Fe^{3+}-containing oxides: $GdBa_2Ca_2Fe_5O_{13}$ (dark grey), $GdBa_2Fe_3O_8$ (red), $GdBaCaFe_3O_8$ (green) and $NaCa_2Fe_3O_7$ (dark blue).

conductive octahedral layers from each other. Because of that the curvature of the VB along the $[001]_p$ direction in GBCFO (b_2 direction in reciprocal space, as represented in Fig. S6) is almost zero, resulting in large effective masses for charge carriers and hence making the $[001]_p$ direction highly unfavorable for electronic conduction in GBCFO. Similar behavior is observed for the acceptor doped $GdBa_2Fe_3O_8$ and $NaCa_2Fe_3O_7$ compounds (Fig. 8); the only difference from GBCFO is the nature of insulating layer - it is either FeO_4 tetrahedra (in $NaCa_2Fe_3O_7$) or FeO_5 pyramids (in $GdBa_2Fe_3O_8$).

4. Conclusions

DFT+U calculations on the $GdBa_2Ca_2Fe_5O_{13}$ perovskite-related oxide exposed a distinct band structure that reveals a 2D-electronic behavior. The computing methodology (GGA+U approximation) used in this work captures both the nuclear and magnetic structures of the compound. The crystal structure, which consists of layered Gd/Ba/Ca ordering in combination with the ordering of three different coordination-polyhedra around the Fe-atoms (FeO_6-octahedra, FeO_5-squared pyramids and FeO_4-tetrahedra), causes a peculiar contribution of the differently located Fe and O atoms to the resulting band structure. Both the valence and the conduction bands are shown to be spatially distributed in the lattice depending on the oxygen-coordination of the Fe atoms. In particular, the bottom of the CB is formed by 3d orbitals of Fe atoms possessing $3z^2 - r^2$ symmetry, which are located within the FeO_5-squared pyramids. However, the electronic states near the Fermi level are mainly formed by 2p states of oxygen atoms occupying the equatorial positions of the FeO_6-octahedra. As a result, $GdBa_2Ca_2Fe_5O_{13}$ appears to be a narrow-gap 2D-semiconductor (the respective band gap E_g is found to be $\sim$0.5 eV) where the FeO_5-layers create the CB, the FeO_6-layers form the VB and the FeO_4-layers create insulating channels avoiding the intralayer transport of electrons. The existence of the three types of oxygen-coordination around the Fe-atoms seems to be essential for the narrow band gap, since other possible double combinations of oxygen-polyhedra forming the anion sublattice, as well as singular ones lead to higher E_g values. The computed pCOHP curves conclude a strongly bonding character of the chemical interaction between all the Fe atoms and the oxygens in the oxide and confirm the insulating character of the FeO_4 layers. Computed electronic conductivity tensors support the anisotropic electrical properties of the $GdBa_2Ca_2Fe_5O_{13}$, since the conductivity is established within the (*ab*)-planes (*i.e.* $(001)_p$ planes), but it is about four orders of magnitude lower along the *c*-axis ($[001]_p$ direction) of the structure. Overall, the band-structure of the $GdBa_2Ca_2Fe_5O_{13}$ oxide is a consequence of the existence and ordering of the three different types of FeO_x polyhedra within the crystal structure.

Conflicts of interest

There are no conflicts to declare.

Data availability

The data supporting this article have been included as part of the supplementary information (SI). Supplementary information: structural and magnetic data of various oxides used in the DFT+U calculations (Table S1); graphic representations of $GdBaCaFe_3O_8$, $GdBa_2Fe_3O_8$ and $NaCa_2Fe_3O_7$ crystal structures (Fig. S1); graphic representations of disordered $GdBa_2Ca_2Fe_5O_{13}$ crystal structures (Fig. S2); computed energy-volume curve for the $GdBa_2Ca_2Fe_5O_{13}$ oxide and the respectively derived Debye temperature and unit cell volume dependences on temperature (Fig. S3); optimized coordinates of the G-AFM $GdBa_2Ca_2Fe_5O_{13}$ unit cell (Table S2); comparison of GGA+U computed densities of states for $GdFeO_3$ ferrites with and without accounting for the 4f states of Gd atoms (Fig. S4); GGA+U computed optical spectra for the G-AFM $GdBa_2Ca_2Fe_5O_{13}$ oxide (Fig. S5); computed band dispersions of the orthorhombic $GdBa_2Ca_2Fe_5O_{13}$ unit cell with G-AFM magnetic ordering (Fig. S6); charge density projections of the CB and VB of the G-AFM $GdBa_2Ca_2Fe_5O_{13}$ along the $[100]_p$ direction (Fig. S7); GGA+U computed band dispersion and experimentally measured optical absorption spectrum of $CaBaFe_4O_8$ oxide (Fig. S8); DOS/pDOS spectra of $GdFeO_3$, $BaCaFe_2O_5$ and $CaBaFe_4O_8$ as obtained within the GGA+U framework (Fig. S9); graphic representation of the allocation of different point defects in $GdBa_2Ca_2Fe_5O_{13}$ crystal lattice (Fig. S10). See DOI: **https://doi.org/10.1039/d5cp01780g**.

Acknowledgements

This research has been supported by the ''Plan de Recuperación, Transformación y Resiliencia-C17.I1'' with funds from the European Union – Next Generation EU, ''European Regional Development Fund'' as part of the action after the COVID-19 pandemic, and Comunidad de Madrid with the project ''GREEN H2-CM''. Authors also thank MCIN/AEI/10.13039/501100011033 for funding the Project PID2022-139039OB-C22 and MCIN/AEI/10.13039/501100011033/''NextGenerationEU''/PRTR for funding the Project TED2021-130452B-C21. Special thanks to Mikhail Kalinkin from the Institute of Solid State Chemistry UB RAS for measuring optical spectra.

References

1 T. Ishihara, Inorganic Perovskite Oxides, in *Springer Handbook of Electronic and Photonic Materials*, ed. S. Kasap and P. Capper, Springer, Cham, 2017.
2 T. Wolfram and S. Ellialtioglu, *Electronic and optical properties of d-band perovskites*, Cambridge University Press, Cambridge, 2006.
3 D. I. Khomskii, *Transition metal compounds*, Cambridge University Press, Cambridge, 2014.
4 M. Nasir, I. Kim, K. Lee, S. I. Kim, K. H. Lee and H. J. Park, *Phys. Chem. Chem. Phys.*, 2023, **25**(5), 3942–3949.
5 J. Ding and X. Zhu, *J. Mater. Chem. C*, 2024, **12**, 9510–9561.

6 J. Irvine, J. L. Rupp, G. Liu, X. Xu, S. Haile and X. Qian, *et al.*, *JPhys Energy*, 2021, **3**(3), 031502.
7 G. R. Monama, K. E. Ramohlola, E. I. Iwuoha and K. D. Modibane, *Results Chem.*, 2022, **4**, 100321.
8 X. Liang, W. Yan, Y. Yu, K. Zhang, W. An and H. Chen, *et al.*, *Angew. Chem., Int. Ed.*, 2023, **62**(46), e202311606.
9 A. N. Zainon, M. R. Somalu, A. M. K. Bahrain, A. Muchtar, N. A. Baharuddin, S. A. Muhammed Ali, O. Nafisah, A. S. Abdullah, A. Abul Kalam and P. B. Nigel, *et al.*, *Int. J. Hydrogen Energy*, 2023, **48**(53), 20441–20464.
10 S. E. Wolf, F. E. Winterhalder, V. Vibhu, L. B. de Haart, O. Guillon, R. A. Eichel and N. H. Menzler, *J. Mater. Chem. A*, 2023, **11**(34), 17977–18028.
11 W. Zhang and Y. H. Hu, *Catal. Today*, 2023, **409**, 71–86.
12 S. Baratov, E. Filonova, A. Ivanova, M. B. Hanif, M. Irshad and M. Z. Khan, *et al.*, *J. Energy Chem.*, 2024, **94**, 302–331.
13 E. Tezel, D. Guo, A. Whitten, G. Yarema, M. Freire and R. Denecke, *et al.*, *J. Electrochem. Soc.*, 2022, **169**(3), 034532.
14 A. I. Klyndyuk, E. A. Chizhova, D. S. Kharytonau and D. A. Medvedev, *Materials*, 2022, **15**, 141.
15 J. A. Kilner and M. Burriel, *Annu. Rev. Mater. Res.*, 2014, **44**(1), 365–393.
16 J. H. Kim and A. Manthiram, *J. Mater. Chem. A*, 2015, **3**(48), 24195–24210.
17 F. Fauth, E. Suard, V. Caignaert, B. Domenges, I. Mirebeau and L. Keller, *Eur. Phys. J. B*, 2001, **21**, 163–174.
18 Z. Gao, L. V. Mogni, E. C. Miller, J. G. Railsback and S. A. Barnett, *Energy Environ. Sci.*, 2016, **9**(5), 1602–1644.
19 P. Winiarz, E. A. Sroczyk, A. Brzoza-Kos, P. Czaja, K. Kapusta and K. Świerczek, *Acta Mater.*, 2024, **277**, 120186.
20 A. A. Taskin, A. N. Lavrov and Y. Ando, *Prog. Solid State Chem.*, 2007, **35**(2–4), 481–490.
21 D. Parfitt, A. Chroneos, A. Tarancón and J. A. Kilner, *J. Mater. Chem.*, 2011, **21**(7), 2183–2186.
22 R. Pelosato, G. Cordaro, D. Stucchi, C. Cristiani and G. Dotelli, *J. Power Sources*, 2015, **298**, 46–67.
23 D. Muñoz-Gil, D. Pérez-Coll, E. Urones-Garrote, U. Amador and S. García-Martín, *J. Mater. Chem. A*, 2017, **5**(24), 12550–12556.
24 D. Muñoz-Gil, E. Urones-Garrote, D. Pérez-Coll, U. Amador and S. García-Martín, *J. Mater. Chem. A*, 2018, **6**(13), 5452–5460.
25 D. Muñoz-Gil, D. Ávila-Brande, E. Urones-Garrote and S. García-Martín, *Dalton Trans.*, 2015, **44**(23), 10867–10874.
26 S. García-Martín, K. Manabe, E. Urones-Garrote, D. Ávila-Brande, N. Ichikawa and Y. Shimakawa, *Inorg. Chem.*, 2017, **56**(3), 1412–1417.
27 P. Karen, *J. Solid State Chem.*, 2021, **299**, 122147.
28 P. Karen, E. Suard and F. Fauth, *Inorg. Chem.*, 2005, **44**(23), 8170–8172.
29 J. M. Hudspeth, D. J. Goossens, A. J. Studer, R. L. Withers and L. Norén, *J. Phys.: Condens. Matter*, 2009, **21**(12), 124206.
30 R. Marín-Gamero, X. Martinez de Irujo-Labalde, E. Urones-Garrote and S. García-Martín, *Inorg. Chem.*, 2020, **59**(8), 5529–5537.
31 X. M. de Irujo-Labalde, U. Amador, C. Ritter, M. Goto, M. A. Patino, Y. Shimakawa and S. García-Martín, *Inorg. Chem.*, 2021, **60**(11), 8027–8034.
32 G. Kresse and J. Furthmüller, *Computational Materials Physics, Faculty of Physics*, Universitat Wien, 2014.
33 J. Sun, A. Ruzsinszky and J. P. Perdew, *Phys. Rev. Lett.*, 2015, **115**(3), 036402.
34 H. D. Saßnick and C. Cocchi, *Electron. Struct.*, 2021, **3**(2), 027001.
35 J. He and C. Franchini, *Phys. Rev. B: Condens. Matter Mater. Phys.*, 2012, **86**(23), 235117.
36 S. L. Dudarev, G. A. Botton, S. Y. Savrasov, C. J. Humphreys and A. P. Sutton, *Phys. Rev. B: Condens. Matter Mater. Phys.*, 1998, **57**(3), 1505.
37 J. K. Shenton, D. R. Bowler and W. L. Cheah, *J. Phys.: Condens. Matter*, 2017, **29**(44), 445501.
38 L. Wang, T. Maxisch and G. Ceder, *Phys. Rev. B: Condens. Matter Mater. Phys.*, 2006, **73**(19), 195107.
39 M. Alaydrus, I. Hamada and Y. Morikawa, *Phys. Chem. Chem. Phys.*, 2021, **23**(34), 18628–18639.
40 M. Gómez-Toledo, S. A. López-Paz, S. García-Martín and M. E. Arroyo-de Dompablo, *Inorg. Chem.*, 2023, **62**(8), 3445–3456.
41 M. Ferri, J. Elliott, S. Fabris and S. Piccinin, *Phys. Rev. B*, 2020, **101**(15), 155201.
42 B.-L. Liu, Y.-C. Wang, Y. Liu, Y.-J. Xu, X. Chen, H.-Z. Song, Y. Bi, H.-F. Liu and H.-F. Song, *J. Chem. Phys.*, 2023, **158**, 084108.
43 A. Otero-De-La-Roza, D. Abbasi-Pérez and V. Luaña, *Comput. Phys. Commun.*, 2011, **182**(10), 2232–2248.
44 X. M. de Irujo-Labalde, M. Goto, E. Urones-Garrote, U. Amador, C. Ritter and M. Amano-Patino, *et al.*, *Chem. Mater.*, 2024, **36**(10), 5184–5191.
45 A. Demont, M. S. Dyer, R. Sayers, M. F. Thomas, M. Tsiamtsouri and H. N. Niu, *et al.*, *Chem. Mater.*, 2010, **22**(24), 6598–6615.
46 C. Tenailleau, M. Allix, J. B. Claridge, M. Hervieu, M. F. Thorpe and R. J. Cava, *J. Solid State Chem.*, 2003, **176**(2), 381–392.
47 X. M. de Irujo-Labalde, E. Urones-Garrote and S. García-Martín, *Solid State Sci.*, 2024, **151**, 107516.
48 O. A. Salawu, S. Boulfrad and U. Schwingenschlögl, *J. Mater. Chem. A*, 2016, **4**(9), 3560–3564.
49 M. F. Hoedl, C. Ertural, R. Merkle, R. Dronskowski and J. Maier, *J. Phys. Chem. C*, 2022, **126**(30), 12809–12819.
50 M. Gajdoš, K. Hummer, G. Kresse, J. Furthmüller and F. Bechstedt, *Phys. Rev. B: Condens. Matter Mater. Phys.*, 2006, **73**(4), 045112.
51 V. Wang, N. Xu, J. C. Liu, G. Tang and W. T. Geng, *Comput. Phys. Commun.*, 2021, **267**, 108033.
52 R. Dronskowski and P. E. Blöchl, *J. Phys. Chem.*, 1993, **97**, 8617–8624.
53 G. K. Madsen, J. Carrete and M. J. Verstraete, *Comput. Phys. Commun.*, 2018, **231**, 140–145.
54 P. E. Blöchl, O. Jepsen and O. K. Andersen, *Phys. Rev. B: Condens. Matter Mater. Phys.*, 1994, **49**(23), 16223.
55 H. Weihe and H. U. Güdel, *Inorg. Chem.*, 1997, **36**(17), 3632–3639.
56 T. Katsura and Y. Tange, *Minerals*, 2019, **9**(12), 745.

57 R. Marín Gamero, *Óxidos metálicos con superestructura derivada de la perovskita y estudio de sus propiedades electrocatalíticas en la reducción de oxígeno*, 2024.
58 A. Scrimshire, A. Lobera, A. M. T. Bell, A. H. Jones, I. Sterianou, S. D. Forder and P. A. Bingham, *J. Phys.: Condens. Matter*, 2018, **30**(10), 105704.
59 S. Lutfalla, V. Shapovalov and A. T. Bell, *J. Chem. Theory Comput.*, 2011, **7**(7), 2218–2223.
60 P. Adler, U. Schwarz, K. Syassen, A. P. Milner, M. P. Pasternak and M. Hanfland, *J. Solid State Chem.*, 2000, **155**(2), 381–388.
61 M. Capone, C. J. Ridley, N. P. Funnell, M. Guthrie and C. L. Bull, *Phys. Status Solidi B*, 2021, **258**(2), 2000413.
62 E. Marelli, J. Lyu, M. Morin, M. Leménager, T. Shang and N. S. Yüzbasi, *et al.*, *EES Catal.*, 2024, **2**(1), 335–350.
63 U. Von Barth and C. D. Gelatt, *Phys. Rev. B: Condens. Matter Mater. Phys.*, 1980, **21**(6), 2222.
64 X. H. Zhu, X. B. Xiao, X. R. Chen and B. G. Liu, *RSC Adv.*, 2017, **7**(7), 4054–4061.
65 V. R. Galakhov, E. Z. Kurmaev, K. Kuepper, M. Neumann, J. A. McLeod and A. Moewes, *et al.*, *J. Phys. Chem. C*, 2010, **114**(11), 5154–5159.
66 X. Bo, D. Wang and X. G. Wan, *Phys. Lett. A*, 2021, **394**, 127202.
67 B. Ouyang, T. Chakraborty, N. H. Perry, T. Mueller, N. R. Aluru and E. Ertekin, *Chem. Mater.*, 2019, **31**(9), 3144–3153.
68 M. D. Scafetta, A. M. Cordi, J. M. Rondinelli and S. J. May, *J. Phys.: Condens. Matter*, 2014, **26**(50), 505502.
69 M. K. Warshi, V. Mishra, A. Sagdeo, V. Mishra, R. Kumar and P. R. Sagdeo, *Ceram. Int.*, 2018, **44**(7), 8344–8349.
70 Encyclopedia Britannica, **https://www.britannica.com/science/color**, (accessed April 2025).
71 *Colorimetry: Understanding the CIE System*, ed. J. Schanda, John Wiley & Sons, 2007.
72 Y. Shin, K. Y. Doh, S. H. Kim, J. H. Lee, H. Bae, S. J. Song and D. Lee, *J. Mater. Chem. A*, 2020, **8**(9), 4784–4789.
73 A. D. Bamburov, A. A. Markov, M. V. Patrakeev and I. A. Leonidov, *Solid State Ionics*, 2019, **332**, 86–92.
74 J. E. Auckett, G. J. McIntyre, M. Avdeev, H. De Bruyn, T. T. Tan, S. Li and C. D. Ling, *J. Appl. Crystallogr.*, 2015, **48**(1), 273–279.
75 I. Kim, H. Lee and M. Choi, *J. Appl. Phys.*, 2022, **131**(7), 075106.
76 V. P. Zhukov and E. V. Chulkov, *Phys. Solid State*, 2022, **64**(4), 422–431.
77 I. A. Leonidov, A. A. Markov, M. A. Zavyalov, O. V. Merkulov, E. V. Shalaeva and S. S. Nikitin, *et al.*, *Materials*, 2022, **15**(13), 4390.